Coalescence and rising behavior of co-axial and lateral bubbles in viscous fluid: A CFD study

P. Ganesan[1,*] Md. Tariqul Islam[1], D. Pokrajac[2], F. A. Hamad[3], Shanti C. Sandaran[4]

[1]Department of Mechanical Engineering, Faculty of Engineering, University of Malaya, 50603, Kuala Lumpur, Malaysia
[2]School of Engineering, University of Aberdeen, Aberdeen AB24 3UE, UK
[3]School of Science and Engineering, Teesside University, Middlesbrough, TS1 3BA UK
[4]University Technology Malaysia, Skudai, Johor, Malaysia

Abstract

The coalescence and rising behavior of co-axial and lateral bubbles in viscous fluid is reported for non-ambient conditions in line with actual operating conditions of industrial bubble column. The volume of fluid with the continuum surface force (VOF-CSF) model embedded in FLUENT CFD package is used. Three main case studies, namely under ambient and aqueous condition ($\mu^* = \sigma^* = 1$), under reduced viscosity ($\mu^* = 0.1$) and surface tension ($\sigma^* = 0.1$) are investigated and compared using two co-axial bubble and three lateral bubble rise configuration models. The latter two cases represent operating conditions at high temperature or pressure. Details of co-axial bubble (or a pair of bubbles rising in a vertical line) and three lateral bubble rise and coalescence characteristics are presented.

Keywords: Volume of fluid (VOF), Bubble, Coalescence, Breakup and Repulsion.

1. Introduction

Gas–liquid bubble columns are commonly used as multiphase reactors in chemical, petrochemical and pharmaceutical industries, etc., for its advantages such as a high mass and heat transfer and an effective inter-phase contact. [1-3] The heat and mass transfer as well as performance of a bubble column depends strongly on the bubble flow dynamics, bubble coalescence and bubble break up phenomenon. [4-6] The details of bubble rise dynamics and coalescence of co-axial and lateral arrangements of individual bubbles is

* Corresponding author: Email: poo_ganesan@um.edu.my

important for better understanding of the bubbly flow in bubble columns. Thus, the present study utilizes computational fluid dynamics (CFD) as a means to investigate details of bubble coalescence mechanism and rising behaviors of two co-axial bubbles (or vertical set-up) and three bubbles lateral arrangements.

A number of experimental studies have been reported on co-axial bubbles (or a pair of bubbles rising in a vertical line) and their coalescence. [7-11] For example, Katz and Meneveau[7] experimentally investigated the rising motion of air bubbles in stagnant water at Reynolds number, $Re = (U\rho_l d_o)/\mu_l$ ranging from 0.2 to 35 and found that the collision between bubbles resulted mainly from wake-induced relative motion. Watanbe and Sanada[9] studied the motion of co-axial bubbles rising in stagnant fluid both experimentally and numerically. They found that the bubbles collided at a low Reynolds number but not at an intermediate Reynolds number which had an equilibrium distance between the bubbles. Lin et al.[10] investigated co-axial bubble coalescence mechanism in a non-Newtonian fluid experimentally and found that shear-thinning effect and viscoelastic effect play key role in the course of bubble coalescence.

A few experimental studies have been carried out to investigate the interactions and coalescence between bubbles in lateral arrangement.[12-17] For example, Sanada et al. [15] investigated the motion and coalescence of two lateral bubbles rising in stagnant water and silicone oil using high speed camera. They found that the coalescence or bounce of the lateral bubbles strongly depended on the critical Reynolds number and Weber number, $We = (\rho_l U^2 d_o)/\sigma$ and the velocity of bubbles decreases after coalescence. The effects of impurities and liquid viscosity on lateral bubbles dynamics have been examined by Figueroaand Zenit[18] and Sanada et al. [19]. Kee and Chhabra[20] reported the coalescence process of two and three lateral bubbles rising in polyacrylamide and carboxymethyl cellulose (CMC) non-Newtonian fluids, respectively. Liu et al. [21] studied the coalescence and interaction of three lateral bubbles at equal distances rising in CMC non-Newtonian fluids using VOF method. It has been found that the three lateral bubbles coalesce when the horizontal distance between the bubbles was less than one millimeter, otherwise the bubbles repulse each other.

Numerical methods such as Volume of Fluid (VOF)[4-6], Lattice Boltzmann (LB)[22-24], and Front Tracking (FT)[25] are quite popular at present for investigating bubble formation and coalescence characteristics as they have the advantage of revealing many fundamental details that cannot be measured. Computational studies are found to provide very reasonable results in comparison with experimental data. For example, Liu et al. [21] found around 7% relative error in comparing between the computational and the experimental data for the bubble rise velocity and the bubble aspect ratio. Gupta and Kumar [23] also used LB method to investigate the effect of vorticity on the oscillating movement and consequent coalescence of multiple bubbles. The authors found that the dynamics of multiple bubbles depends on the leading bubble's vortex structure. Cheng et al. [22] investigated the effect of the density ratio and the initial bubble configuration on the flow field as well as the evolution of bubble shape during coalescence using LB method. They found that the trailing bubble experienced an obvious deformation when it enters the wake region of the leading bubble. Furthermore, for two rising bubbles with different sizes, the larger bubble has strong effect on the smaller bubble for any initial configuration. Hasan et al. [6] used VOF method to investigate a coalescence mechanism of a pair bubble of 0.56 mm size in a viscous fluid and found that the bubble coalescence is enhanced at a higher bubble Bond number, $Bo = (g\rho_l d_o^2)/\sigma$.

Most previous studies in a similar context have been carried out for ambient conditions and aqueous systems despite the fact that industrial bubble columns often operate at high temperature and pressure. Moreover, bubble motions and sizes have been found to be significantly affected by pressure and temperature.[26-30] For example, Schafer et al. [30] investigated bubbly flow in a column at pressures up to 50 bars and temperatures up to 175 ^oC under varied superficial gas velocities and using different N_2/liquid mixtures as sparged gas. They found that the gas density, surface tension, liquid viscosity is influenced by the temperature and the pressure. An increase in temperature and pressure reduces the liquid viscosity and the surface tension significantly while the influence on gas property is less prominent. Lastly, they concluded that the effects of both temperature and pressure reduce stable bubble sizes, which supports the findings of Pohoreckiet al. [28]

The motivation of the present study is to further investigate bubble characteristics under a high pressure and temperature. We have previously studied the effects of the reduced liquid properties on the formation of

a bubble from an orifice[31, 32]. The present study will provide insights into rise and coalescence characteristics of two co-axial air bubbles (i.e. a pair of bubbles rising in a vertical line) and three lateral bubbles at industrial conditions by simulating the effects of reduced viscosity and surface tension.

2. Methodology

2.1 Model setup and boundary conditions

The present study investigates coalescence and rising behavior of air bubbles in stagnant glycerin solution which has a higher liquid viscosity than water in order to ease the presentation the bubble shape changes. The study also includes sensitivity analysis for a series of viscosity and surface tension values which shows that the findings from the present study are representative for various types of liquids, particularly those used in industry including water. The simulation domain is a rectangle; $0 \leq X \leq D$, $0 \leq Y \leq H$,(Fig. 1), where D and H are the width and the height of the domain, respectively, and D=H=100mm. This domain represents 2D cross sectional view of a cylindrical bubble column. Literature data[5, 17, 33, 34] have adopted such domain for observing asymmetry in bubble shape and rise characteristics. Further justification for selecting a 2D domain for the present study is based on findings of Zahedi et al. [33] who reported insignificant difference (max 7%) between 2D and 3D simulations in the bubble velocity and diameter. No slip boundary condition is assigned to the bottom and the two side walls of the domain, whereas pressure outlet boundary condition is prescribed at the top wall. The operating pressure is set to be equal to the atmospheric pressure, i.e., 101325 Pa and the gravitational force acts in the negative Y direction.

Two main configurations of bubbles have been used, one with two co-axial bubbles (Fig. 1a) and the other one with three bubbles in lateral orientation (Fig. 1b). For the former case, a series of different initial spacing between the bubbles ($Y_{initial}$) ranging from 4 to 12 mm was tested. The results for $Y_{initial}$ = 4 to 10 mm were very similar and therefore only the results for $Y_{initial}$=8mm are presented. For $Y_{initial}$ = 12mm, the co-axial bubbles do not coalesce, instead they rise independently. This case has also been omitted as the independent rise is not the focus of the present study. For the both CFD models at beginning of the

simulation the bubbles are located above the bottom wall. The effect of the column walls on the bubble behavior is negligible since the bubble size (4 to 12 mm) is much smaller than the column width.

2.2 Governing equations

2.2.1 Continuity and momentum equation

The governing equations of continuity and momentum for an incompressible Newtonian fluid can be written as

$$\nabla.\vec{V} = 0 \tag{1}$$

$$\rho\left\{\frac{\partial\vec{v}}{\partial t} + \nabla.(\vec{V}\vec{V})\right\} = -\nabla P + \nabla.\left[\mu\left\{\nabla\vec{V} + (\nabla\vec{V})^{T}\right\}\right] + \rho\vec{g} + \vec{F}s \tag{2}$$

Where $\vec{V}$, P, ρ, μ and $\vec{F}s$ are the velocity vector, pressure, fluid density, fluid viscosity and volume force due to surface tension respectively.

2.2.2 VOF equation

The volume of fluid (VOF) utilizes the volume ratio function, *F*; which is defined as the ratio of volume of the principal fluid to the total volume in each cell or grid. The principal fluid in this study is liquid, so *F* is 0 for a cell full of gas, 1 for a cell full of liquid, and 0 <*F*< 1 for a cell that contains a gas-liquid interface. The gas-liquid interface boundary is tracked by solving the volume fraction continuity equation [35]

$$\frac{\partial F}{\partial t} + \vec{V}.\nabla F = 0 \tag{3}$$

2.2.3 Additional scalar equation for calculation of the material properties

The fluid material properties for a computational cell are calculated as

$$\rho = \rho_l F + \rho_g[1 - F] \tag{4}$$

$$\mu = \mu_l F + \mu_g[1 - F] \tag{5}$$

where subscripts *l* and *g* denote liquid and gas, respectively.

2.2.4 Continuum surface force (CSF) equation

The continuum surface force (CSF) which represents the gas-liquid interfacial tension is incorporated as a source term in the momentum equation (Eq. 2) by introducing a volume force $\vec{F}_S$ as described by Brackbill et al. [36]. This volume force is calculated as

$$\vec{F}_S = \frac{\sigma \rho k \nabla F}{0.5\,(\rho_l + \rho_g)} \tag{6}$$

where, k is the surface curvature of the interface which is defined in terms of divergence of the unit vector, $\hat{n}$ and it is calculated by using the following equations

$$k = -(\nabla . \hat{n}) = \frac{1}{|\vec{n}|}\left[\left(\frac{\vec{n}}{|\vec{n}|} \cdot \nabla\right)|\vec{n}| - (\nabla \cdot \vec{n})\right], \text{ where } \hat{n} = \frac{\vec{n}}{|\vec{n}|} \tag{7}$$

In this study, the piecewise linear interface calculation (PLIC) method [37]is used to trace the gas and liquid interface reconstruction. [21, 38]

2.3 Numerical procedures

In the present study, Ansys-Fluent [39], which is based on the finite volume method, has been used to solve the governing equations. To minimize the numerical diffusion, the QUICK scheme was applied to solve the momentum equation. The pressure implicit with splitting operators (PISO) algorithm was used for the pressure-velocity coupling. The PISO algorithm allows a rapid convergence rate without a significant loss of the solution stability and accuracy.[40] The pressure has been solved using the PRESTO! scheme. The transient model, which is based on an explicit scheme, used a time step of 0.0001s. Under-relaxation factor of 0.3 and 0.7 was set for the pressure and momentum, respectively to assist the convergence. The scaled residual of 1×10^{-7} was set as the convergence criteria for all the governing equations.

2.4 Simulation cases

Bubble column in actual industry is often used under high temperature and pressure operating conditions [26, 28, 30] which can significantly change the characteristics of the bubble.[26, 28, 30] It is known fact that the viscosity and surface tension of the liquid reduce with the increase of temperature and pressure. Therefore, the aim of the present study is to identify some of changes in bubble characteristics under the

reduced viscosity and surface tension conditions in comparison to those at typical ambient conditions and for aqueous systems.

A total of five simulations (or 81cases) were carried out and the details are shown in Table 1. The non-dimensional viscosity (μ^*) and surface tension (σ^*) are given as the ratio between the reduced value (μ_r or σ_r) to its value at room temperature (μ_l or σ_l). Further details of the simulation cases are presented below.

(a) Validation cases (Simulation 1):

Cases 1-12 were used to validate the CFD methods and to investigate the effect of Morton number on bubble rise dynamics for 4-10mm bubble diameters. Three different types of glycerin/water mixtures (namely G1, G2 and G3) with different viscosity and density values were used for the simulations. The surface tension is about 0.064 N/m for all the mixtures. All values of fluid properties were obtained from experimental study of Raymond & Rosant.[38]

(b) Reduced viscosity (Simulation 2):

The effect of reducing liquid viscosity on the behaviour of two co-axial bubbles is investigated (Cases 13-30) using of one of the glycerin/water mixtures (namely, G3). The liquid viscosity is reduced from 0.076 to 0.0076 Pa.s coresponding to μ^*=1 to 0.1. Three bubble diameters - 4, 6 and 8mm are tested.

(c) Reduced surface tension (Simulation 3):

Similarly, Cases 31-45 are used to investigate the effect of reducing surface tension based on the model of two co-axial bubbles. The surface tension is reduced from 0.064 to 0.0064 Pa.s coresponding to σ^*=1 to 0.1. Three bubble diameters - 4, 6 and 8mm are tested.

(d) Collision of three lateral bubbles (Simulation 4):

Simulation four (or Cases 46-63) has been carried out to determine the critical gap between three lateral bubbles for bubble coalescene for six different bubble sizes ranging from 3 to 8mm. Three types of property conditions are tested, one under room temperature ($\mu^* = \sigma^* = 1$), and the other two under the reduced visocity (μ^*=0.1) and surface tension (σ^*=0.1).Trial and error method was used to identify the critical initial flat gap for the start of bubble coalescence. The non-dimensional critical lateral gap ($S_c = \Delta x_c/d_b$) is defined as the ratio between the critical lateral gap for bubble coalescence (Δx_c) and the initial bubble diameter (d_b). This definition is adopted from Liu et al. [21]

(e) No-collision of three lateral bubbles (Simulation 5):

Lastly, Cases 64-81 have been used to investigate the repulsion behavior of the bubbles when the initial lateral gap between them is larger than the critical gap S_c. Three non-dimensional lateral gaps ($S= \Delta x/d_b$) of 0.5, 1 and 1.5 are tested for 4,6 and 8 mm bubble diameters under three types of property conditions (i.e., $\mu^* = \sigma^* = 1$; $\mu^*=0.1$; $\sigma^*=0.1$).

2.5 Model validation

2.5.1 Grid analysis

A uniform structured mesh (Fig. 1c) is used everywhere in the domain. The effect of mesh size was investigated for four grid step sizes i.e., 0.18 mm, 0.22 mm, 0.25 mm and 0.30 mm. Mesh dependencies have been tested for a 4 mm and 8 mm bubble initially located at the centre of the bottom of the domain, in glycerin solution. The density, viscosity and surface tension coefficient of the fluid (G3) was 1205 kg/m^3, 0.076 Pa.s and 0.063 N/m, respectively[38]. Fig. 2 shows the bubble rise velocity versus time for the four different step sizes. The velocities are almost identical for the step size of 0.18 mm and 0.22 mm, whereas a small deviation is observed for the 0.25 mm and moderate deviation for 0.3 mm mesh. The 0.22 mm mesh was therefore adopted for the present study in order to minimize the computing time without compromising the accuracy of the results.

2.5.2 Code validation

Validation of the numerical simulations was carried out by comparison with the literature data for two cases. The first case involves the coalescence of two lateral bubbles in silicone oil, with initial bubbles' diameter and spacing between them of 1.8 mm and 0.2 mm respectively. The experimental results for this case are reported in Duineveld[11], Sanada et al. [15], and numerical simulation using moving particle semi-implicit (MPS) method is presented in Chen et al.[41]. Density, viscosity and surface tension of silicone oil were 817 kg/m^3, 8.17×10^{-4} and 0.0169 N/m, respectively. Fig. 3 shows the coalescence process of two lateral bubbles computed in the present study using VOF method along with the experimental results of Duineveld[11] and Sanada et al.[15], as well as the MPS simulations of in Chen et al.[41]. The bubbles' topologies from both

numerical simulations agree very well with the experiments, with VOF showing slightly better agreement. The VOF method is able to simulate the formation of curvature of the vapor bridge (at 0.0073s), which increases surface tension and hence causes the rapid expansion of the merged bubble in vertical direction and shrinking in lateral direction. The lower surface then begins to move upwards slower than upper surface, thus altering the bubble shape which becomes bullet-like at 0.0135s.

For the second validation, a single air bubble of four different initial sizes (4, 6, 8 and 10 mm) was imposed in three different viscous fluids - G1, G2 and G3 (see Table 1:Simulation 1). The results were compared with the experimental data from Raymond & Rosant[38]. Fig. 4 shows the quantitative comparison between the simulation results for Cases of 1-12 and the experimental data.[38] It shows that the bubble terminal velocity increases with the increase of the bubble size in three different viscous fluids (i.e., G1, G2, and G3). Comparison between experimental data[38] and the present simulation shows, on average, reasonably close agreement. Some differences (i.e., less than 12% relative error) are observed for 8 mm and 10 mm bubbles.

Fig. 5 illustrates the bubble aspect ratio as a function of bubble diameter. The bubble aspect ratio is calculated as the ratio of the bubble height (h) to width (w) after the bubble has reached steady conditions (i.e. there are no more changes in the bubble shape). The solid lines correspond to the curves fitted to the experimental data of Raymond & Rosant[38]. The agreement between the present simulation and the experimental data [38]is very good, with maximum relative error less than 6%. It is observed that as the bubble size increases the bubble aspect ratio decreases, hence indicating the change of bubble shape from spherical into ellipsoidal. Additionaly, the above results from Figs. 4 and 5 represent the effect of Morton number, $Mo=(g\mu_l^4/\rho_l\sigma^3)$ on bubble behavior: a bubble rises more quickly and deformes more in low Mo number fluid (G3) , compared to higher Mo number fluidsg G1 and G2. The more pronounced deformation occurs due to higher differential pressure between the upper and lower surface of bubble.

In summary, the above comparison between experiments, correlation results and the simulation results indicates that the present CFD method is capable of predicting bubble rise and coalescence accurately. The validated method was then used for investigating the effects of liquid viscosity and surface tension as well as the initial gap between lateral bubbles on co-axial and lateral bubble coalescence.

3. Results and discussion

3.1 Co-axial bubbles coalescence

3.1.1 Effect of liquid viscosity

The effect of non-dimensional liquid viscosity ($\mu^* = \mu_r/\mu_l$) on the two co-axial bubble coalescence and the change in bubbles' shape is discussed. Fig. 6 illustrates the bubble coalescence time as a function of the non-dimensional liquid viscosity, μ^*. In general, the bubble coalescence time (t_{BC}) decreases with the decrease of μ^*: a gradual reduction is seen for μ^* from 1.0 to 0.25 but a steep reduction occurs for μ^*= 0.25 to 0.10. The steep reduction of t_{BC} occurs due to low resistance of fluid which results in a quick interaction between the two bubbles. For a particular bubble diameter, the bubbles' shape prior to coalescence process for different μ^* is almost identical, with a much enhanced shape at μ^*=0.1. At a specific μ^*, e.g., μ^* = 0.1, the following bubble (or trailing bubble) of 4, 6, 8mm has ellipsoidal shape, oblate ellipsoidal cap shape and skirted shape, respectively. This change of shape for different bubble size occurred due to stronger drag of liquid on larger bubbles.

3.1.2 Effect of surface tension

Fig. 7 illustrates the time at which bubble coalesce (t_{BC}) for different non-dimensional surface tension (σ^*). In general, t_{BC} decreases with the decrease of σ^* for all the bubble sizes. The change in t_{BC} is not significant from σ^* = 1 to 0.3 for all bubbles. A steep reduction occurs for σ^* less than 0.3 but the changes are more significant for 4 mm bubble. In other words, the effect of σ^* is only limited to a small value of σ^* and a small bubble (4mm). Compare the shape the leading and trailing bubbles of 4mm. At σ^*=1 (higher value), both bubbles are very similar to each other and has an oblate shape. However, with the reduction of σ^*, the leading bubble tends to elongate more in the horizontal direction (i.e., ellipsoidal cap shape) and eventually the leading and the trailing bubble have a completely different shape, e.g., see at σ^*=0.1. This in turn changes the mobility of the bubbles and fastens the coalescence process. The edge of the leading bubbles of 6 and 8mm breaks up into few small bubbles distributed around the trailing bubble. At σ^*=0.1 the trailing bubble of 4, 6 and 8mm bubbles has ellipsoidal cap shape, ellipsoidal cap shape with lateral deformation, and

skirted shape prior to breakup, respectively. For the biggest bubble (8mm), low resistance to shape change due to the reduced surface tension causes a break-up of the trailing bubble.

3.2 Rise characteristics of three lateral bubbles

3.2.1 Lateral coalescence mechanism and breakup

Fig. 8 shows the non-dimensional critical flat gap, S_c, of bubble coalescence for different initial bubble sizes, liquid viscosities, μ^*, and surface tensions, σ^*. Note that S_c represents the maximum initial gap at which bubbles coalesce. In general S_c reduces with the increase of the bubble size. For all bubble sizes reducing μ^* from 1 to 0.1 results in about 13% increase in S_c, whereas reducing σ^* from 1 to 0.1 decreased S_c by around 54%. The latter result implies that bubbles can be distributed closer to each other under a reduced surface tension condition in comparison to the reference case.

The evolution of the shape, lateral coalescence and breakup of the three lateral bubbles initially at S_c condition is shown in Fig. 9, for different bubble sizes, μ^* and σ^*. First compare 4 mm and 6 mm initial bubble size at the original condition ($\mu^* = \sigma^* = 1$) shown in Figs. 9a and 9b (the top two), respectively. For 4 mm (Fig. 9a), the three lateral bubbles merge to form a single flat bubble (at t = 0.020s) which eventually deforms into an ellipsoidal shape at 0.13s. This observation is consistent with that reported for two lateral bubbles by Sanada et al.[15] (experimetal work) and Chen et al.[41] (CFD simulations). For 6mm bubble (Fig. 9b), a V-shaped bubble not seen for 4mm bubble develops at t = 0.042. At t = 0.081s, the bubble adopts a dumb-bell shape which finally breaks into two daughter bubbles at t = 0.091s. The relative liquid velocity vector surrounding the dumb-bell shape bubble (6mm) at t = 0.081s is shown in Fig. 10a. On the top surface of the bubble, the velocity is quite uniformly distributed, with parallel, upward pointing vectors covering almost entire width. On the left and right sides of the bubble, the velocity has a circular direction (anti-clock and clock wise respectively) indicating a downward motion. Relatively strong upward liquid jet can be seen around the middle of the underneath part of the bubble. As a result, the left and right parts of the bubble rotate in opposite directions hence extending the bridge between them until it eventually ruptures in the middle to form two daughter bubbles which move upwards and away from each other (see Fig. 9b at t=0.091s & 0.130s).

Fig. 9c and 9d compares the effect of using 6 mm and 8 mm bubbles for the case of reduced liquid viscosity, μ^*. The rise characteristics and the bubble shape for the two bubble sizes are quite similar. For the 6mm bubble the initial coalescence is slightly sooner than for 8mm bubble (t = 0.011s compared to t = 0.016s), but the break-up is bit later (t = 0.053s compared to 0.046s). The main difference occurs after the breakup – 6mm bubbles produce two daughter bubbles whereas 8mm bubbles produce three. The middle daughter bubble formed in the latter case (Fig. 9d) has the shape of 'bullet' (at t=0.046s) which also appears for the reduced surface tension, σ^* at t=0.039s (Fig. 9e).

The relative liquid velocity vectors surrounding the bubble shape just before the breakup into two or three daughter bubbles (i.e. at t=0.046s for the 6mm bubble, Fig. 9c, and at t=0.039s for the 8mm bubble, Fig. 9d) are shown in Figs. 10b and 10c, respectively. The shapes of the two bubbles are very different – the one resulting from the 6mm bubbles has two distinct mounds connected by a concave bridge whereas the 8mm bubble has three mounds with two bridges. The flow pattern around the two mounds of 6mm bubble and the two outer mounds of the 8mm bubble are very similar. They are characterized by upward vectors on the top with maximum around the center, combined with counterclockwise and clockwise vectors on the side of the left and right mound, respectively. This rotations, combined with the opposite directions of velocity vectors approaching the bridges (downwards from the top and upwards from the bottom) cause the breakup of the bridges. The middle bubble has upwards velocities close to the top and downwards velocities close to the bottom which continue to elongate the bullet shaped bubble after the breakup.

3.2.2 Repulsive behavior between lateral bubbles

The ratio of the gap between two bubbles and the bubble initial diameter is investigated for the cases of three lateral bubbles rising in a vertical column (Fig. 1b). The non-dimensional distance is given as $\Delta x/d_b$ and $\Delta y/d_b$ for the horizontal and vertical bubble distance. As the initial horizontal distance between two bubbles is set above S_c value, the bubble coalescence will not occur and each bubble will rise independently from the bottom to the top. The rise characteristics (or both $\Delta x/d_b$ and $\Delta y/d_b$) of left and right bubble are symmetrical to the center bubble and therefore only the results for the left side are presented. A small difference between left and right bubble is seen for the case of reduced viscosity but this is ignored as it is not

significant. For all analyzed cases results are presented in the form of time series of $\Delta x/d_b$ and $\Delta y/d_b$ (Fig. 11), contour plots showing the bubbles at various time levels (Fig. 12) and relative velocity vectors (Fig. 13).

3.2.2.1 Ambient condition, ($\mu^* = \sigma^* = 1$)

Referring to Fig. 11a (LEFT), in general, $\Delta x/d_b$ of 4 mm bubble with initial horizontal gaps, S, of 0.5, 1.0 and 1.5 increases as the bubbles rise vertically for the reference case ($\mu^* = \sigma^* = 1$). Increasing $\Delta x/d_b$ indicates that the two side bubbles move away from the middle bubble, see Fig. 12a for example. The profile of $\Delta y/d_b$ value of S=0.5 is quite different from that of S=1.0 and 1.5 as the bubbles rise from the initial value of zero (Fig. 11a, RIGHT). Note that, positive value of $\Delta y/d_b$ indicates that the middle bubble has a higher vertical height than that of the side bubbles and vice versa for –ve $\Delta y/d_b$. The middle bubble of S=0.5 rise faster than the two side bubbles after a slow start until t=0.2s. For S=1.0 and 1.5, the middle bubble is slower than the side bubbles so it remains behind, due to the weaker interaction with the side bubbles, as shown in Fig. 12a.

Now, let us examine the effect of bubble diameter under room operational condition ($\mu^* = \sigma^* = 1$) by comparing Figs. 11a and 11b, LEFT. The profiles of $\Delta x/d_b$ for 4mm and 6mm bubbles, (Figs. 11a and 11b respectively), are quite similar expect for the final $\Delta x/d_b$ value (at t=0.65s) which is longer for 4mm than for 6mm bubble (3.5 compared with 2.8). Referring to Fig. 11b (RIGHT), the profiles of $\Delta y/d_b$ of 6mm bubble for S=0.5, 1.0, 1.5 are similar, with the middle bubble rising slower than side bubbles at the beginning, but eventually catching up and surpassing them (see Fig. 12b for a contour plot). The rate of this change is faster for S=0.5 which is the smallest initial horizontal gap between the bubbles. Comparing Fig. 12a and 12b, 6mm bubble appears to be more ellipsoidal than 4 mm bubble. Referring to the velocity vectors of three lateral 6mm bubbles at t=0.1s (Fig. 13a), there is an outward push to the side bubbles as the middle bubble passes between them. At t=0.5s, see Fig. 13b, the velocities are more uniform and the three bubbles rise independently with the center bubble moving faster (please refer to inset arrows for graphical clarity).

3.2.2.2 Reduced viscosity condition, (μ^* =0. 1)

Referring to Fig. 11c, for 6mm bubble and $\mu^* = 0.1$ $\Delta x/d_b$ generally increases with time, but in a non-uniform fashion – instead it exhibits a wavy behavior. Prior to t = 0.2s, the profile of $\Delta x/d_b$ is very much linked to the initial setup of the lateral gap with some fluctuation in which S = 1.5 case has the highest value in comparison to S = 0.5 and 1 cases. After t = 0.3s, $\Delta x/d_b$ of S = 0.5 case (the shortest lateral gap) increases steeply in short time gap (0.1s) surpassing that of S = 1 and 1.5 cases. This results in the largest final increment for the smallest initial gap between the bubbles, S = 0.5, and smallest for the largest gap, S=1.5. Referring to Fig.11c (RIGHT), the profiles of $\Delta y/d_b$ for S = 0.5, 0.1, 1.5 are quite similar, with the middle bubble having a late start and then shooting up, compared to the side bubbles. Fig. 12c shows a rapid change and non-uniformity in bubble shapes, orientations and positions as the simulation time progresses. Figs. 13c and 13d show the velocity vector of three lateral 6mm bubbles at t=0.1s and t=0.5s, respectively. There is a non-uniform outward push to the side bubbles, which may be due to their non-uniform shape, as the middle bubble passes between them. At t=0.5s, the non-uniform velocity vectors at the bottom of the bubbles imply that the bubbles rise with continuous changes in orientation. As a consequence vortices are formed, especially at the bottom of the side bubbles.

Compare the cases of reduced viscosity ($\mu^* = 0.1$) with the cases at ambient condition ($\mu^* = \sigma^* = 1$) by referring to Fig. 11c ($\mu^* = 0.1$) and Fig. 11b ($\mu^* = 1$). With reduced viscosity $\Delta x/d_b$ increases in a more complex, non-monotonic manner than for $\mu^* = 1$. For S=1.5 the final value of $\Delta x/d_b$, near the outlet, is shorter by 27% for $\mu^* = 0.1$, compared to $\mu^* = 1$. Vertical distance between the bubbles $\Delta y/d_b$ is almost three times higher for the reduced viscosity than for the ambient condition. Unlike in Fig. 12b (for $\mu^* = 1$), the changes in the bubble distribution, orientation and shape in the cases of reduced viscosity shown in Fig. 12c are quite fast, with the shapes of the middle and side bubbles being quite different.

Let us now investigate the effect of bubble diameter (6 versus 8mm) under reduced viscosity ($\mu^* = 0.1$) condition by referring to Figs. 11c & 11d (Distance plot) and also Figs. 12c & 12d (Contour plot). For the two cases the $\Delta x/d_b$ profiles are quite similar, but this is not the case for $\Delta y/d_b$ profiles. For 8mm, the change of $\Delta y/d_b$ (or the bubble rise in vertical direction) is very slow, and the middle bubble surpasses the

side bubble only at much later time (t=0.4s). Compared to 6mm bubble, the change of 8mm bubble shape is quite random, with some bubbles being more elongated (wobbling shape) and some not.

3.2.2.3 Reduced surface tension condition, (σ^* =0. 1)

Referring to Fig. 11e (LEFT) for 8 mm bubble, $\Delta x/d_b$ for σ^*= 0.1 cases increase quite slowly and maintain around 14% differences between different S values (S = 0.5 versus S = 1, and S = 1 versus S = 1.5) throughout simulations time. Fig.11e (RIGHT) shows $\Delta y/d_b$ for the reduced surface tension cases for S = 0.5, 0.1, 1.5, which increase in a similar way with the middle bubble shooting up earlier in comparison to the side bubbles, see Fig. 12e for a contour plot. For example for S = 0.5 case, $\Delta y/d_b$ is about 20% higher on average than for S = 1.5. From Fig. 12e, it is also clear that the change of bubble shape is faster from circular to the ellipsoidal cap shape and begin to break up (t = 0.2s) as a number of small daughter bubbles from edges of the cap shape up to top of the column. These types of bubble break up may enhance the mixing as well as heat and mass transfer rate between gas and liquid phase.

Compare the cases of reduced surface tension (σ^* = 0.1) with the case at ambient condition ($\mu^* = \sigma^*$ = 1) by referring to Fig. 11e (σ^*= 0.1) and Fig. 11f (σ^*= 1) of 8 mm bubble. In general, $\Delta x/d_b$ of the reduced surface tension cases increase monotonically in comparison to that of σ^*= 1 cases. $\Delta y/d_b$ of the reduced surface tension cases is almost two, two and five times higher than that of the ambient condition cases for S = 0.5, 1.0 and 1.5, respectively at outlet (typically t = 0.65s). In addition, an ellipsoidal shape of bubbles at ambient condition ($\mu^* = \sigma^*$ = 1) were observed in comparisons to the cases of reduced surface tension (σ^* = 0.1).

4. Conclusions

In this study, co-axial bubbles (i.e. a pair of bubbles rising in a vertical line) and three lateral bubbles rise and coalescence characteristics have been investigated, using VOF-CSF computational method. Results for reduced viscosity and surface tension conditions which represent an actual industrial high pressure-high

temperature bubble column setup were compared with those obtained for reference ambient conditions. The conclusions from this study are:

- For co-axial bubble coalescence, it is found that the bubble coalescence occurs earlier (i.e., around 20% for μ* and 8.2% for σ*) for the cases with a reduced μ* and σ*. A faster coalescence of bubbles occurs at μ* < 0.25 and at σ* < 0.25.
- The shape of trailing bubble shows a noticeable changes (to an ellipsoidal, oblate ellipsoidal cap and skirted shape) when the diameter of the bubble increases in the reduced μ* and σ* fluid.
- For the three lateral bubbles coalescence, the non-dimensional critical lateral gap of the bubble coalescence decreased with the increase of bubble diameter for the reduced σ* fluid but increased for the reduced μ* fluid. Subsequently, the coalescing of three lateral bubbles broke up into two daughter bubbles when the bubble diameter was increased from 4 mm to 6 mm. When the diameter of three lateral bubbles was further increased to 8 mm in reduced μ* and/or σ* the three daughter bubbles formed again.
- When the initial lateral gaps of bubble were larger than the critical lateral gap of bubble coalescence, the two side bubbles moved apart from the middle bubble due to the repulsive effect. The normalized vertical and horizontal distance between the bubbles varied significantly for increased bubble diameter and reduced liquid viscosity due to the velocity flow field structure.

Acknowledgements

This research is financially supported by University of Malaya, Ministry of Higher Education High Impact Research (UM.C/HIR/MOHE/ENG/20), and Fundamental Research Grant Scheme (FRGS: FP052-2015A).

References

1. M. Pourtousi, J. Sahu and P. Ganesan, *Chemical Engineering and Processing: Process Intensification*, 2014, 75, 38-47.
2. A. A. Kulkarni and J. B. Joshi, *Industrial & engineering chemistry research*, 2005, 44, 5873-5931.
3. M. Pourtousi, P. Ganesan and J. Sahu, *Measurement*, 2015.
4. M. Islam, P. Ganesan, J. Sahu and F. Hamad, *Asia-Pacific Journal of Chemical Engineering*, 2015.
5. M. Pourtousi, P. Ganesan, A. Kazemzadeh, S. C. Sandaran and J. Sahu, *Chemometrics and Intelligent Laboratory Systems*, 2015, 147, 111-120.
6. N. Hasan, *International Journal of Heat and Fluid Flow*, 2011, 32, 755-761.
7. J. Katz and C. Meneveau, *International journal of multiphase flow*, 1996, 22, 239-258.

8. A. De Vries, A. Biesheuvel and L. Van Wijngaarden, *International journal of multiphase flow*, 2002, 28, 1823-1835.
9. M. Watanabe and T. Sanada, *JSME International Journal Series B*, 2006, 49, 410-418.
10. T. J. Lin and G. M. Lin, *The Canadian Journal of Chemical Engineering*, 2003, 81, 476-482.
11. P. Duineveld, in *In Fascination of Fluid Dynamics*, Springer, 1998, pp. 409-439.
12. Y. Hallez and D. Legendre, *Journal of Fluid Mechanics*, 2011, 673, 406-431.
13. J. R. Vélez-Cordero, D. Sámano, P. Yue, J. J. Feng and R. Zenit, *Journal of Non-Newtonian Fluid Mechanics*, 2011, 166, 118-132.
14. W. FAN, Y. MA, X. LI and H. LI, *Chinese Journal of Chemical Engineering*, 2009, 17, 904-913.
15. T. Sanada, A. Sato, M. Shirota and M. Watanabe, *Chemical Engineering Science*, 2009, 64, 2659-2671.
16. A. Zhang and Y. Xiong-Liang, *Chinese Physics B*, 2008, 17, 927.
17. M. T. Islam, P. Ganesan and J. Cheng, *RSC Advances*, 2015, 5, 7819-7831.
18. B. Figueroa-Espinoza and R. Zenit, *Physics of Fluids (1994-present)*, 2005, 17, 091701.
19. T. Sanada, M. Watanabe and T. Fukano, *Chemical engineering science*, 2005, 60, 5372-5384.
20. D. De Kee and R. Chhabra, *Rheologica acta*, 1988, 27, 656-660.
21. J. Liu, C. Zhu, T. Fu, Y. Ma and H. Li, *Chemical Engineering Science*, 2013, 93, 55-66.
22. M. Cheng, J. Hua and J. Lou, *Computers & Fluids*, 2010, 39, 260-270.
23. A. Gupta and R. Kumar, *International Journal of Heat and Mass Transfer*, 2008, 51, 5192-5203.
24. Z. Yu, H. Yang and L.-S. Fan, *Chemical Engineering Science*, 2011, 66, 3441-3451.
25. M. van Sint Annaland, W. Dijkhuizen, N. Deen and J. Kuipers, *AIChE Journal*, 2006, 52, 99-110.
26. T. J. Lin, K. Tsuchiya and L. S. Fan, *AIChE Journal*, 1998, 44, 545-560.
27. X. Luo, D. Lee, R. Lau, G. Yang and F. Liang-Shih, *American Institute of Chemical Engineers. AIChE Journal*, 1999, 45, 665.
28. R. Pohorecki, W. Moniuk, A. Zdrójkowski and P. Bielski, *Chemical engineering science*, 2001, 56, 1167-1174.
29. P. M. Wilkinson and L. L. v. Dierendonck, *Chemical Engineering Science*, 1990, 45, 2309-2315.
30. R. Schäfer, C. Merten and G. Eigenberger, *Experimental Thermal and Fluid Science*, 2002, 26, 595-604.
31. M. T. Islam, P. B. Ganesan, J. N. Sahu and S. C. Sandaran, *The Canadian Journal of Chemical Engineering*, 2015, 93, 1869-1879.
32. T. Islam, P. Ganesan, J. Sahu and F. Hamad, *Thermal Science*, 2015, 15-15.
33. P. Zahedi, R. Saleh, R. Moreno-Atanasio and K. Yousefi, *Korean Journal of Chemical Engineering*, 2014, 1-13.
34. J. Liu, C. Zhu, T. Fu and Y. Ma, *Industrial & Engineering Chemistry Research*, 2014, 53, 4850-4860.
35. C. W. Hirt and B. D. Nichols, *Journal of computational physics*, 1981, 39, 201-225.
36. J. Brackbill, D. B. Kothe and C. Zemach, *Journal of computational physics*, 1992, 100, 335-354.
37. D. Youngs, *Numerical methods for fluid dynamics*, 1982, 24, 273-285.
38. F. Raymond and J.-M. Rosant, *Chemical Engineering Science*, 2000, 55, 943-955.
39. I. Fluent, *Fluent documentation*, 2006.
40. A. Akhtar, V. Pareek and M. Tadé, *Chemical Product and Process Modeling*, 2007, 2.
41. R. Chen, W. Tian, G. Su, S. Qiu, Y. Ishiwatari and Y. Oka, *Chemical Engineering Science*, 2011, 66, 5055-5063.

LIST OF FIGURES

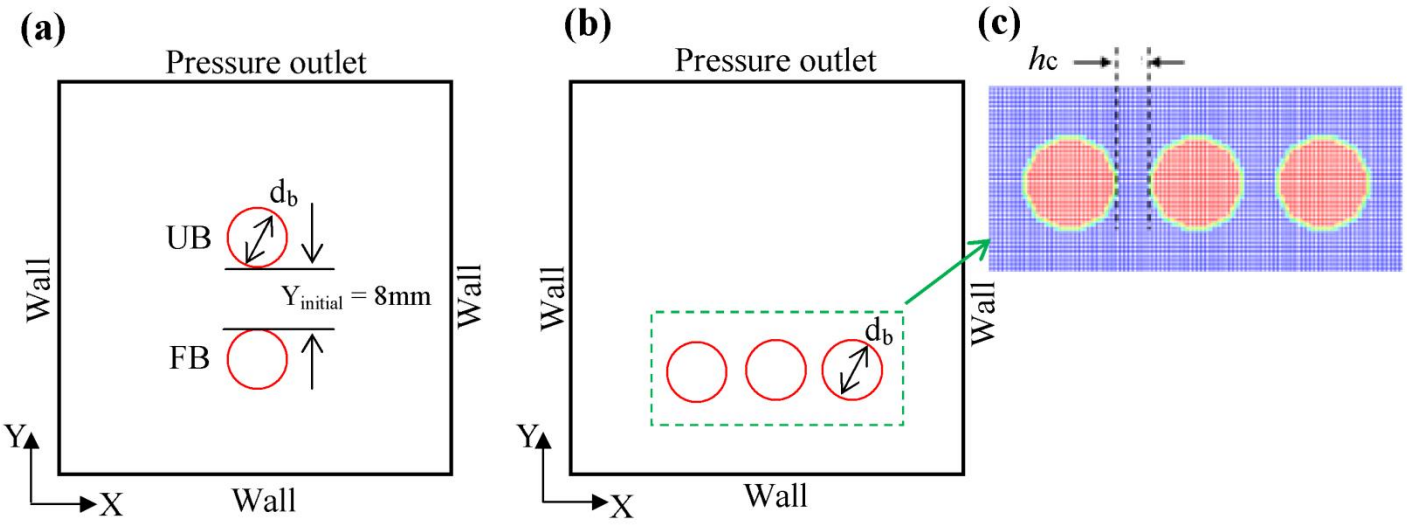

Fig. 1: Computational domain of (a) co-axial bubble; (b) lateral bubble and (c) zoom view near the lateral bubbles. *Noted*: UB and FB means upper and following bubble, respectively.

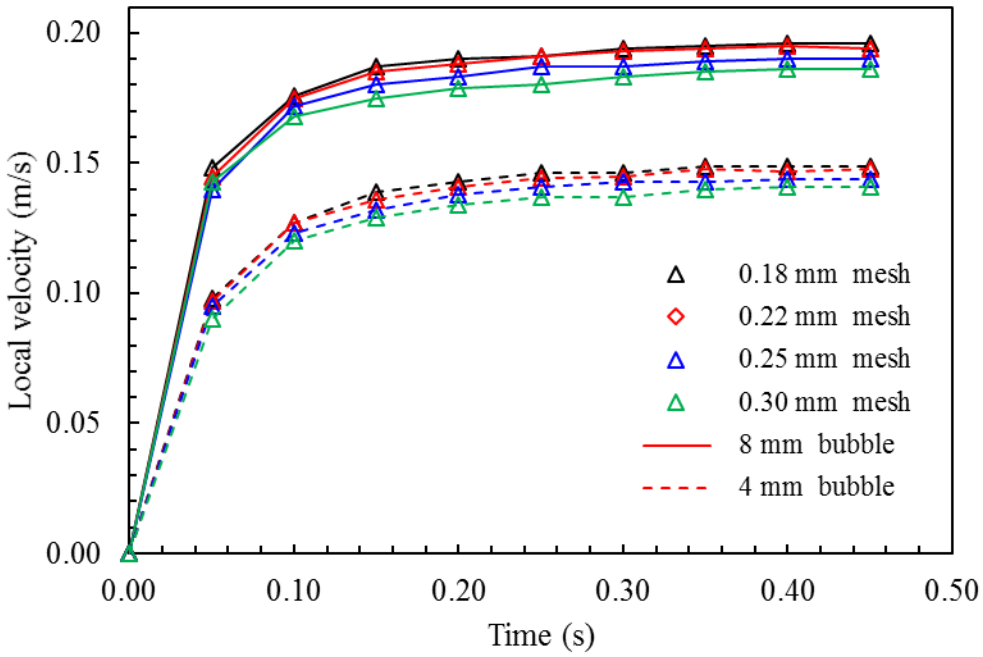

Fig. 2: Mesh dependency study of 4 mm and 8 mm bubble rising velocity at different size of mesh.

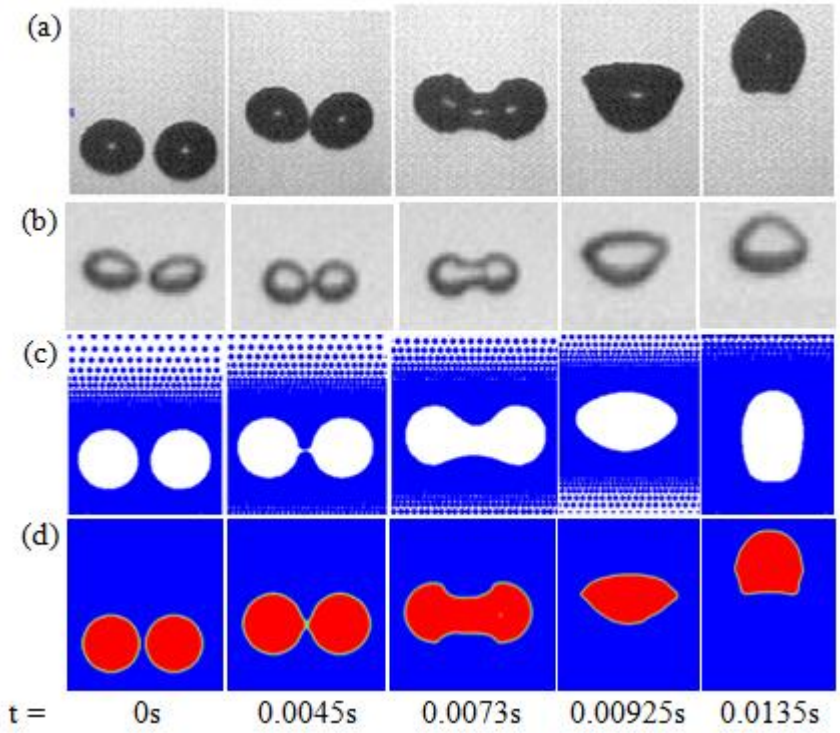

Fig. 3: Observations of coalescence process of two lateral bubbles (a) experiment by Duineveld[11]; (b) experiment by Sanada et al.[19]; (c) MPS method by Chen et al. [41] (d) and present VOF method.

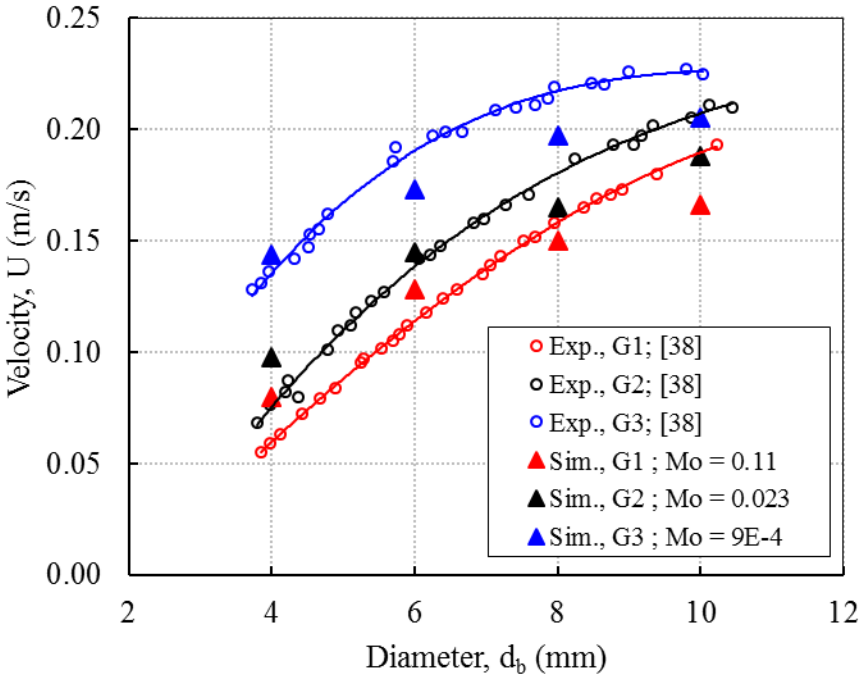

Fig. 4: Terminal velocity as a function of bubble diameter.

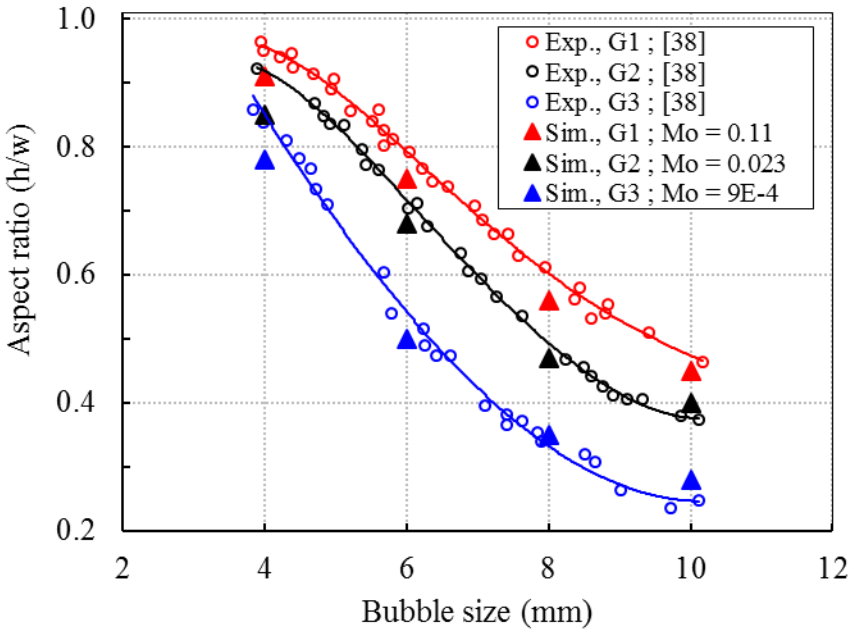

Fig. 5: Bubble aspect ratio as a function of bubble diameter.

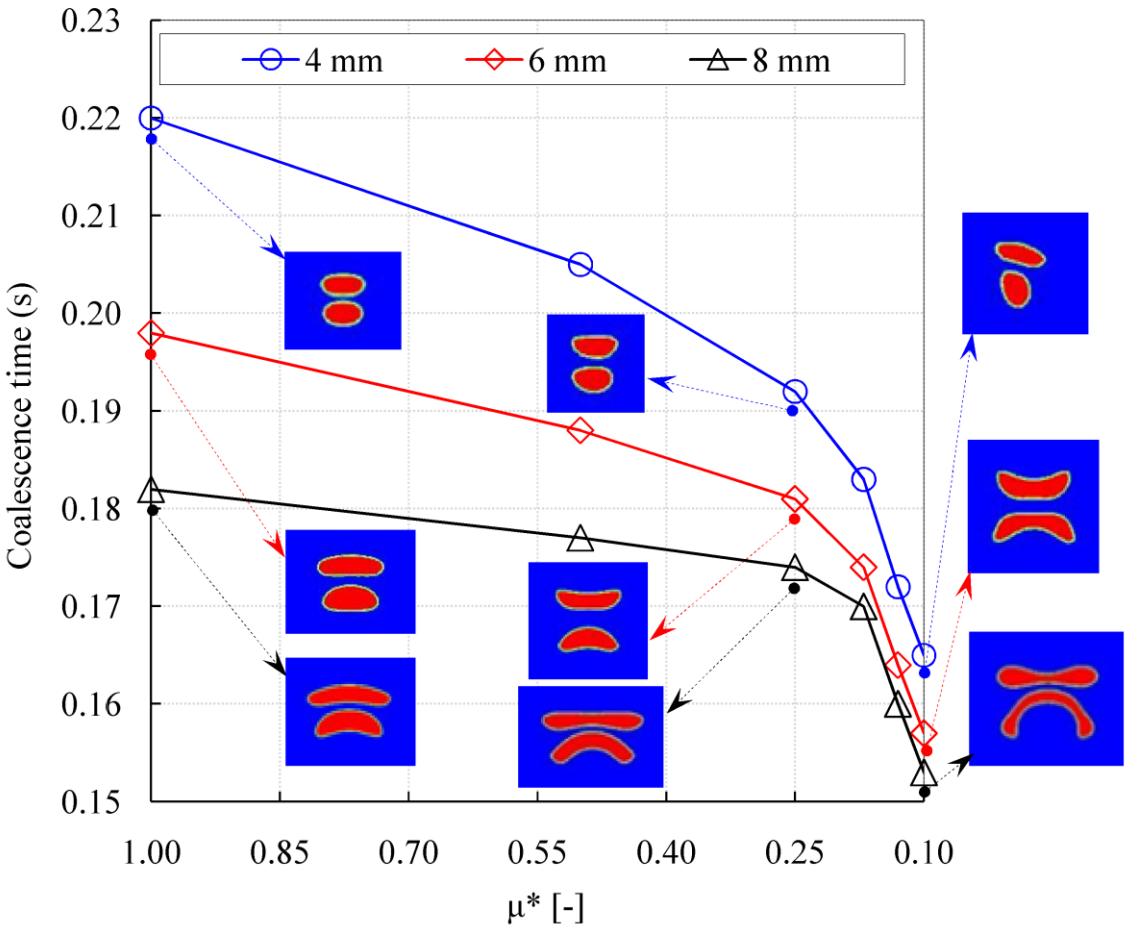

Fig. 6: Bubble coalescence time as a function non-dimensional liquid viscosity, (μ*) for σ* = 1. Insets represent the bubbles image prior to coalescence.

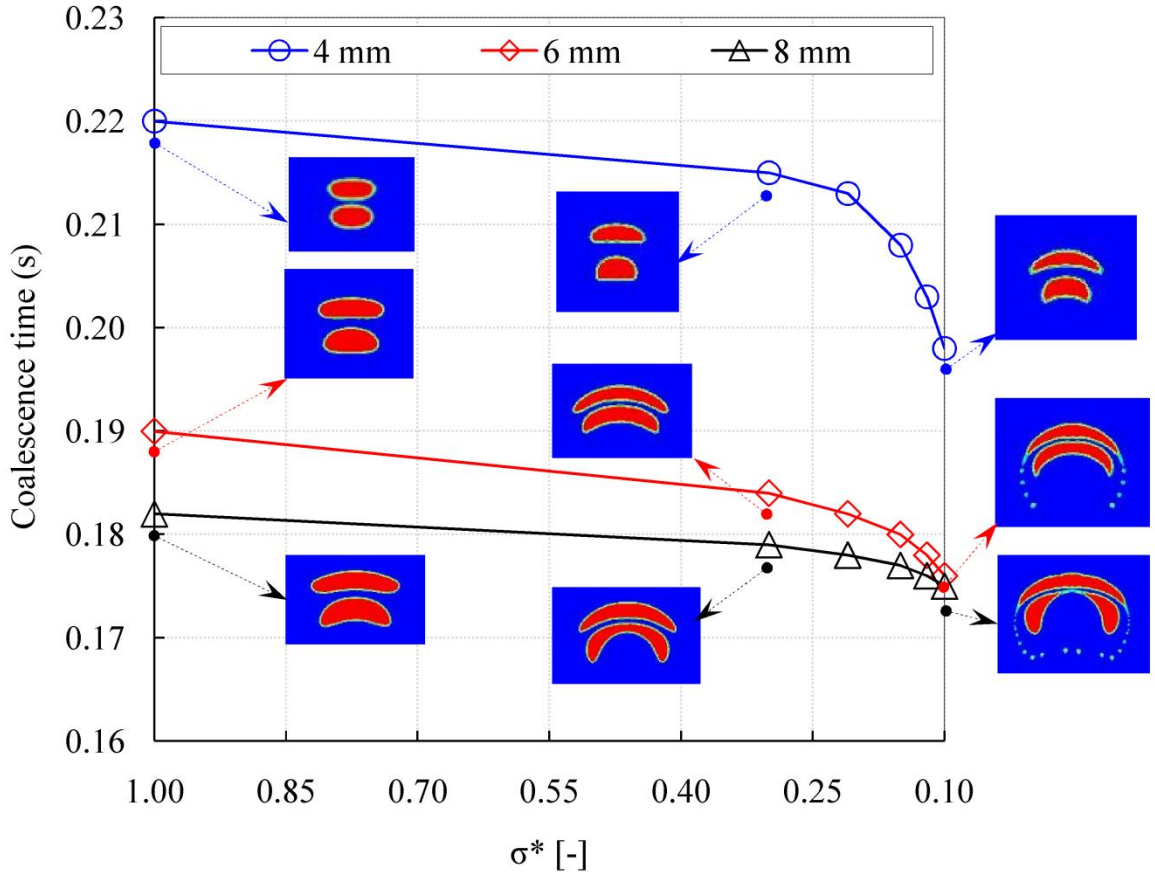

Fig. 7: Bubble coalescence time as a function non-dimensional surface tension, (σ^*) for $\mu^* = 1$. Insets represent the bubbles image prior to coalescence.

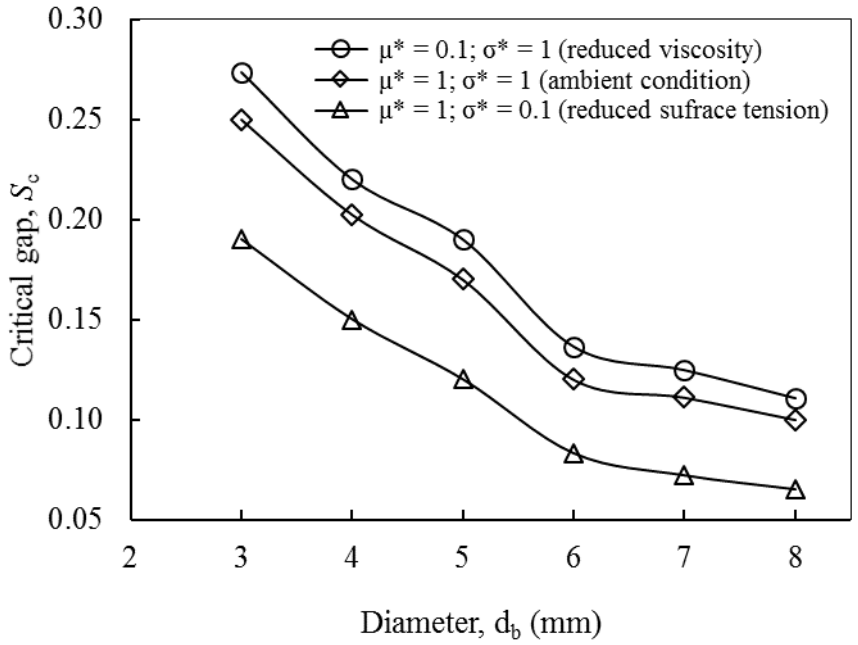

Fig. 8: Non-dimensional critical lateral gap of bubble coalescence as function of bubble diameter.

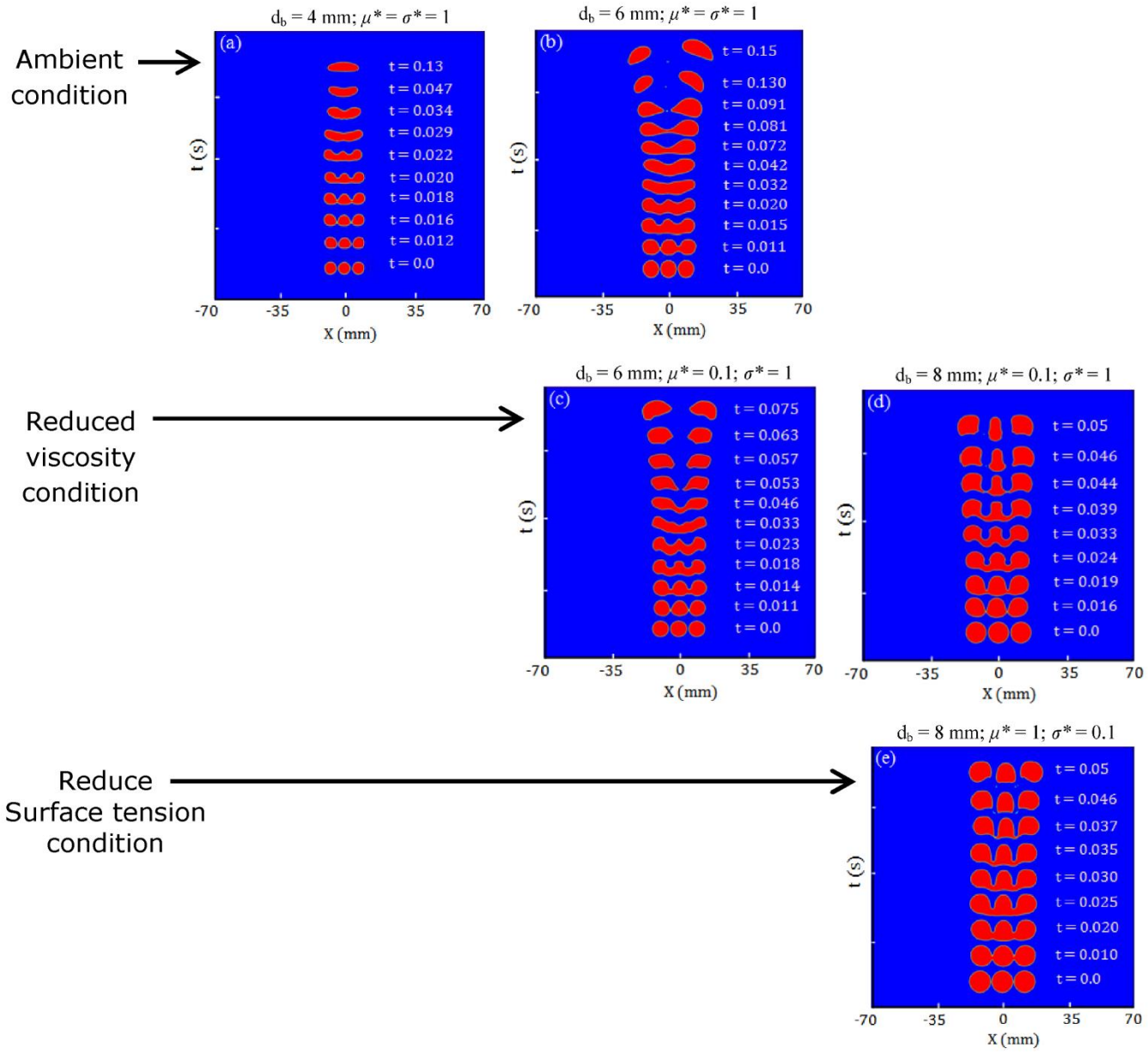

Fig. 9: Three lateral bubble coalescence at condition of *ambient condition* [(a) S_c = 0.2025 or h_c = 0.812 mm, (b) S_c = 0.12 or h_c = 0.72 mm]; *reduced viscosity* [(c) S_c = 0.136 or h_c = 0.816 mm, (d) S_c = 0.11 or h_c = 0.88 mm]; *reduced surface tension* [(e) S_c = 0.05 or h_c = 0.40 mm].

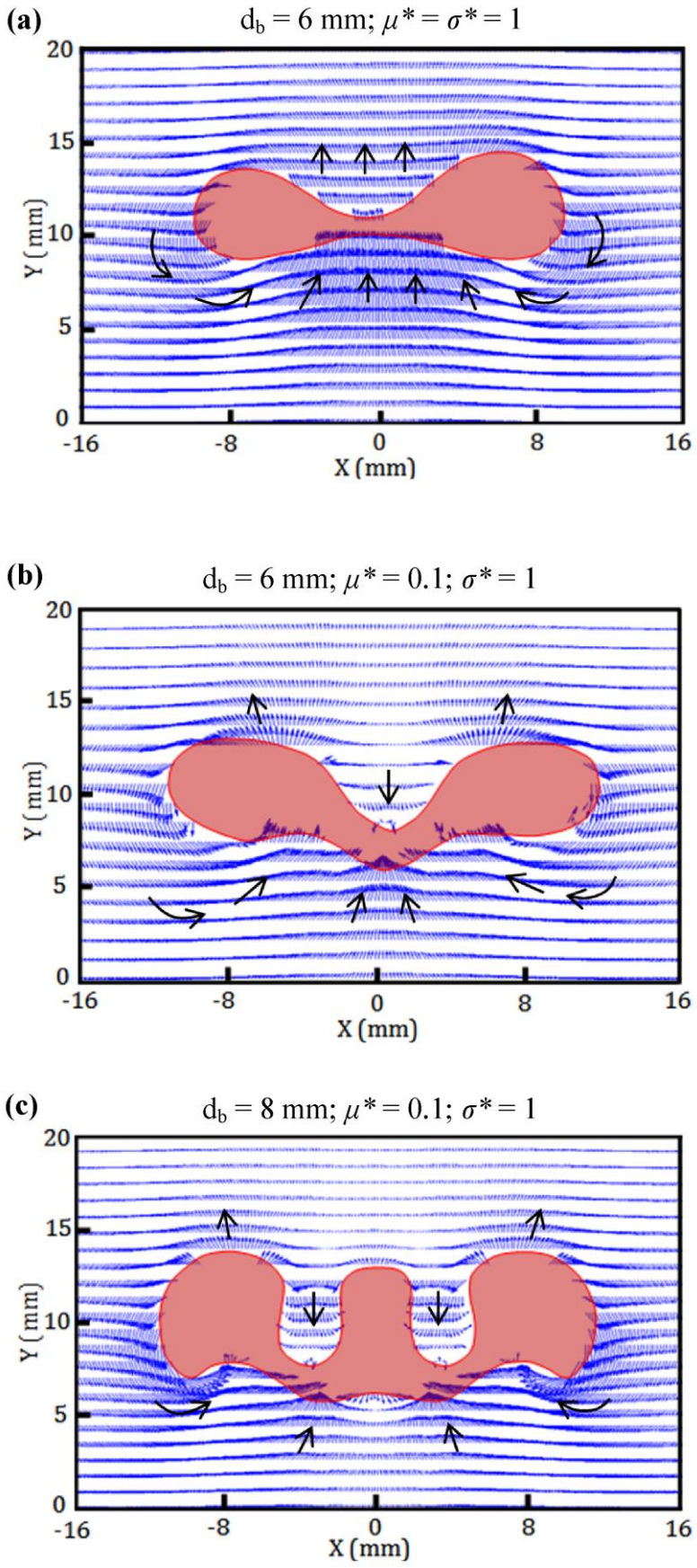

Fig. 10: Relative velocity vector around the coalescing bubble (a) S_c = 0.12 or h_c = 0.72 mm; t = 0.081s; (b) S_c = 0.136 or h_c = 0.816 mm; t = 0.046s; (c) S_c = 0.11 or h_c = 0.88 mm, t = 0.039s.

(a) $d_b = 4$ mm; $\mu^* = \sigma^* = 1$

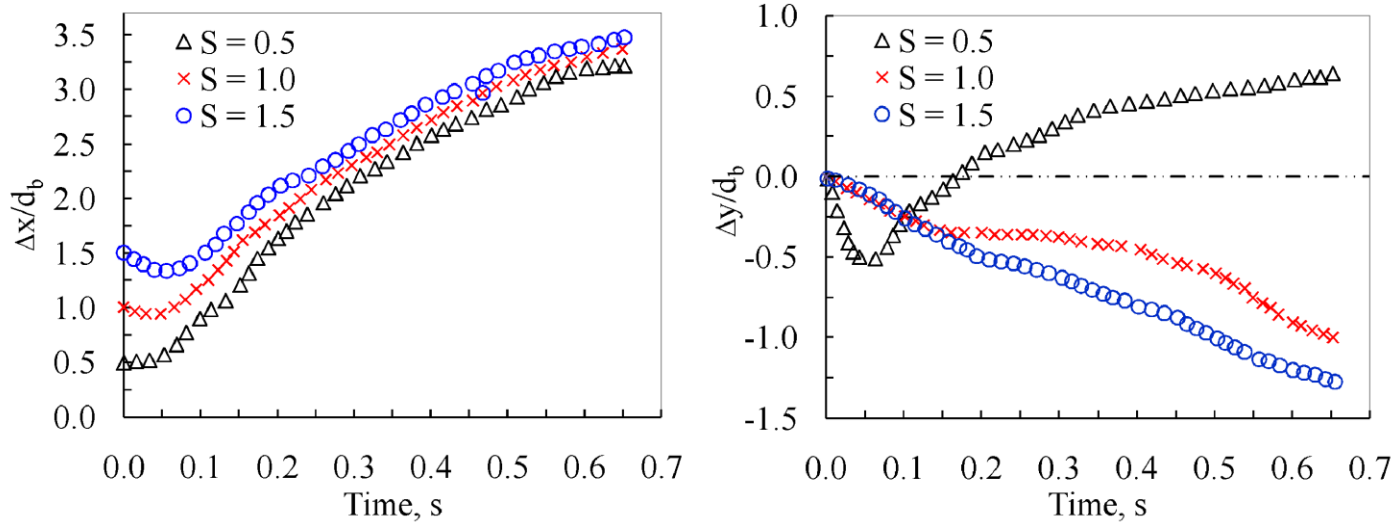

(b) $d_b = 6$ mm; $\mu^* = \sigma^* = 1$

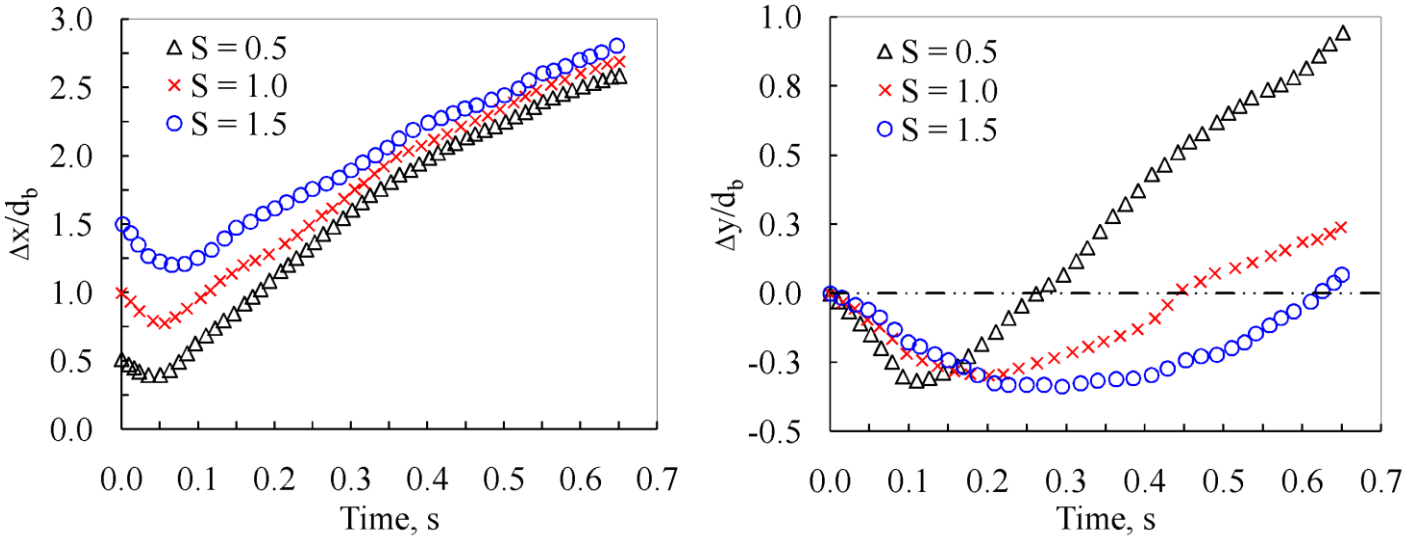

(c) $d_b = 6$ mm; $\mu^* = 0.1$; $\sigma^* = 1$

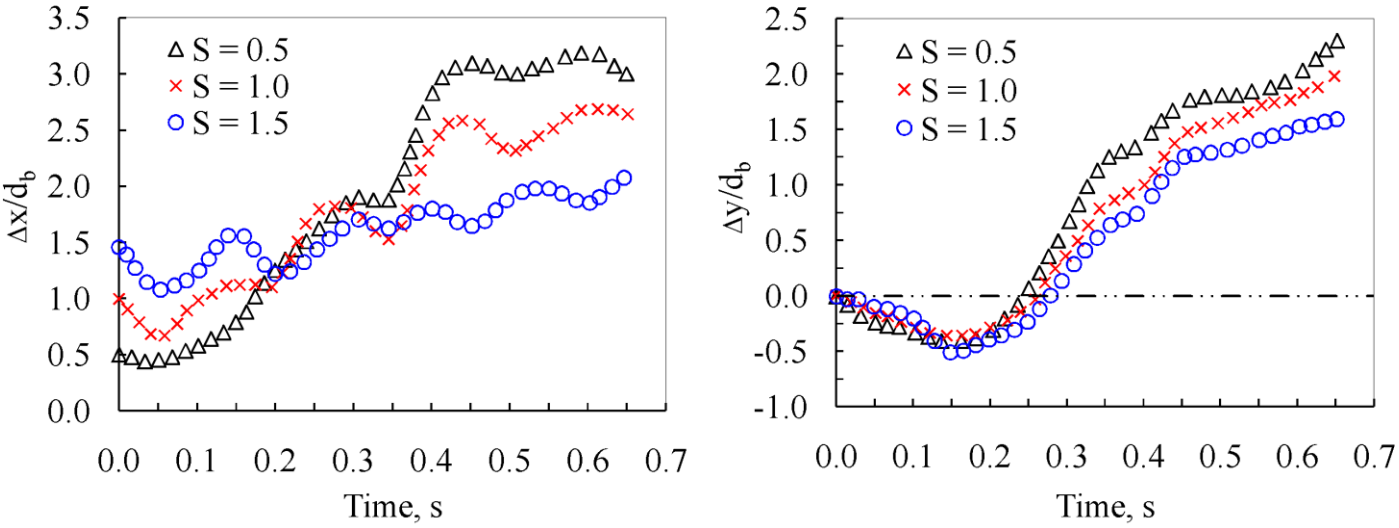

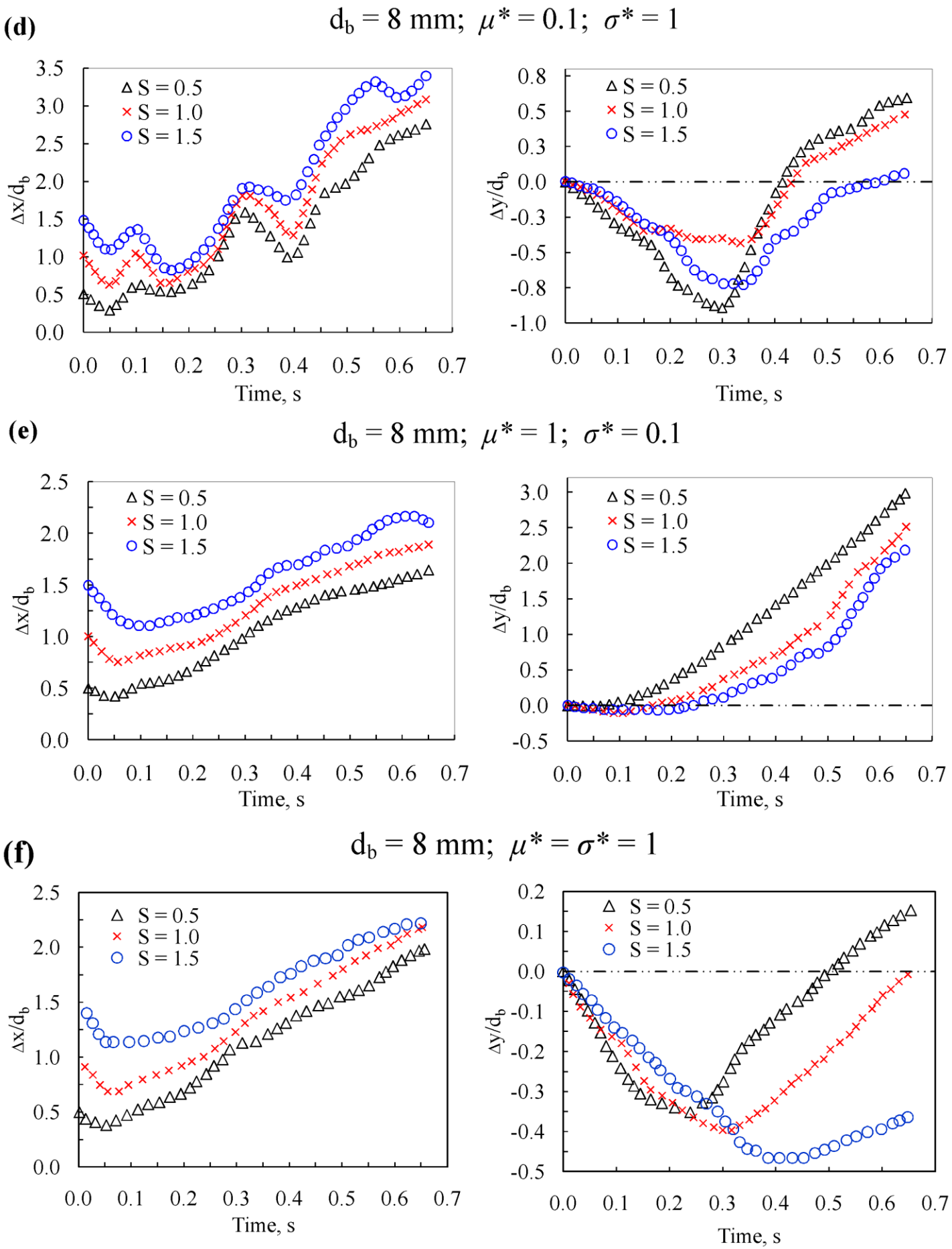

Fig. 11: (a-f) Effect of initial lateral gap (*S*) for different diameters (d_b) of bubble.

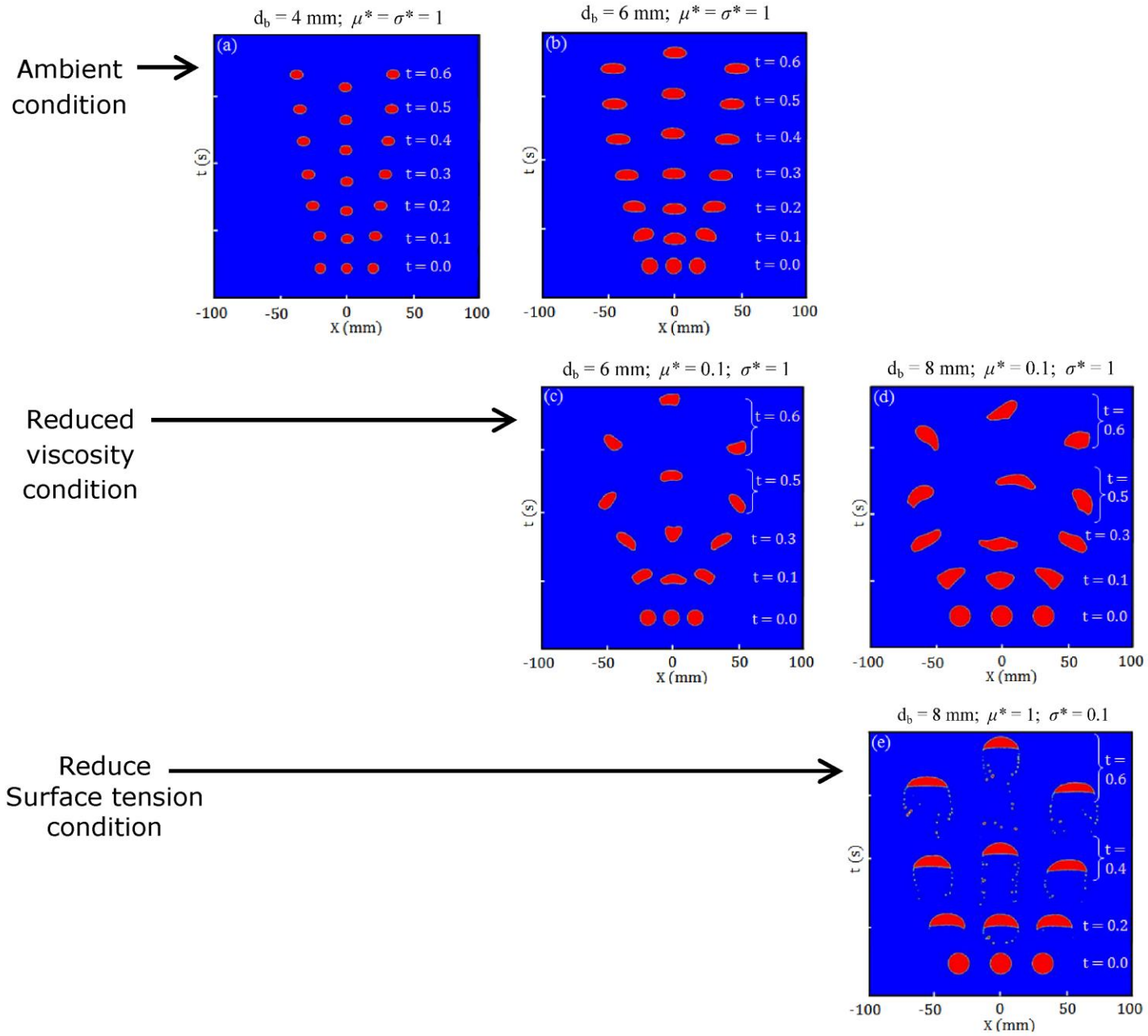

Fig. 12: Three lateral bubble rising trajectories at condition of *ambient condition* [(a) $S = 1.5$, (b) $S = 0.5$]; *reduced viscosity* [(c) $S = 0.5$; (d) $S = 1$]; *reduced surface tension* [(e) $S = 1$].

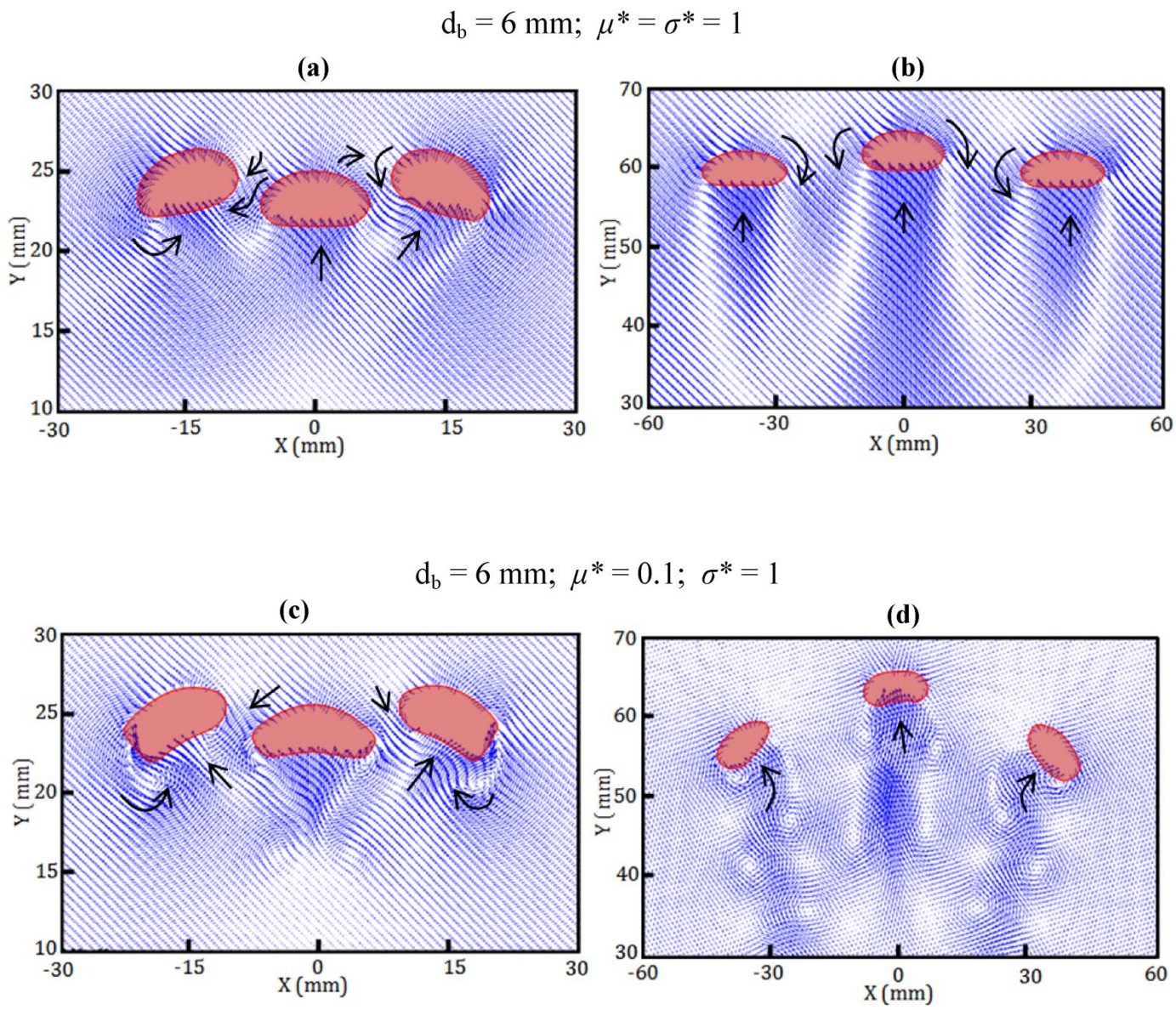

Fig. 13: Relative velocity vector around the bubbles for S = 0.5 at (a) t = 0.1s; (b) t = 0.5s; (c) t = 0.1s; (d) t = 0.5s. Please refer inset arrows for graphical clarity.